Journal of Maps

ISSN: (Print) (Online) Journal homepage: www.tandfonline.com/journals/tjom20

Geology of Tolstoj quadrangle (H08), Mercury

L. Giacomini, L. Guzzetta, V. Galluzzi, L. Ferranti & P. Palumbo

To cite this article: L. Giacomini, L. Guzzetta, V. Galluzzi, L. Ferranti & P. Palumbo (2024) Geology of Tolstoj quadrangle (H08), Mercury, Journal of Maps, 20:1, 2421600, DOI: 10.1080/17445647.2024.2421600

To link to this article: https://doi.org/10.1080/17445647.2024.2421600

JOURNAL OF MAPS
2024, VOL. 20, NO. 1, 2421600
https://doi.org/10.1080/17445647.2024.2421600

Taylor & Francis
Taylor & Francis Group

Science

Geology of Tolstoj quadrangle (H08), Mercury

L. Giacomini[a], L. Guzzetta [b], V. Galluzzi[a], L. Ferranti[c] and P. Palumbo[a]

[a]INAF, Istituto di Astrofisica e Planetologia Spaziali, Rome, Italy; [b]INAF, Osservatorio Astrofisico di Catania, Catania, Italy; [c]DiSTAR, Università degli Studi di Napoli "Federico II", Naples, Italy.

ABSTRACT

Tolstoj quadrangle (H08) is located in the equatorial area of Mercury, between 22.5°N and 22.5° S and 144° and 216°E. Using the NASA/MESSENGER data, we compiled a geological map of the quadrangle at a scale of 1:3.000.000. The main basemap we used was the MDIS 166 m/pixel BDR mosaic. In addition, mosaics with high-incidence illumination from west and east, MDIS global color mosaics, and the MDIS global DEM have been taken into account. In the map, we considered three feature classes: geological units, lineaments, and surface features. Geological units consist of crater material and plains. Lineaments include crater and pit rims, and structures. Finally, surface features are subdivided into crater chains or clusters, hollows, faculae, bright and dark material. The geological map will be integrated into the global 1:3M geological map of Mercury, which is being prepared in support to the ESA/JAXA BepiColombo mission.

ARTICLE HISTORY
Received 24 July 2024
Revised 15 October 2024
Accepted 18 October 2024

KEYWORDS
Mercury; planetary geology; planetary mapping; Tolstoj quadrangle

1. Introduction

Mercury was studied by two different missions: NASA/Mariner10 and NASA/MESSENGER. The first one completed 3 flybys around the planet between 1974 and 1975, covering about 45% of its surface. Based on these images, several geological maps of the planet's surface have been compiled (De Hon et al., 1981; Grolier & Boyce, 1984; Guest & Greeley, 1983; King & Scott, 1990; McGill & King, 1983; Schaber & McCauley, 1980; Spudis & Prosser, 1984; Strom et al., 1990; Trask & Dzurisin, 1984). More than thirty years later, in 2011, MESSENGER entered the orbit of Mercury for a two-year mission. During that period, the MDIS (Mercury Dual Imaging System) instrument acquired images of the surface completing a global coverage of the planet. Thanks to those data, a global geological map of 1:15M was produced (Kinczyk et al., 2019). More recently, an effort to produce quadrangle geological maps at a scale of 1:3M for the entire planet was launched (Galluzzi et al., 2016; Giacomini et al., 2022; Guzzetta et al., 2017;Malliband et al., 2023; Man et al., 2023; Mancinelli et al., 2016; Pegg et al., 2021; Wright et al., 2019). The new geological map series will be useful for the ESA/JAXA (European Space Agency, Japan Aerospace Agency) BepiColombo mission that will reach Mercury in 2026. We present here the geological map of the Tolstoj quadrangle (H08). A previous map of the quadrangle was performed in 1980 at a scale of 1:5M (Schaber & McCauley, 1980). However, it covers about 60% of the quadrangle's area, since the western sector was in darkness in the Mariner10 images. Therefore, the map of this work represents the first complete geologic survey of H08, at 1:3M scale.

2. Data

2.1. Basemaps

The main basemap used for H08 was the MDIS (Mercury Dual Imaging System) and BDR (Basemap reduced Data Record) products. BDRs are mosaics of both WAC (wide-angle camera) and NAC (narrow-angle camera) images at the spatial resolution of 166 m/pixel. They include images with low emission angles at moderate- to high-incidence angles, conditions that best highlight the topography. The images were assembled in several mosaics to have four tiles for each quadrangle (NE, SE, SW and NW). Since we considered a 5° overlap with the surrounding quadrangles (i.e. H03-H04-H07-H09-H12-H13) to allow a globally consistent interpretation of the geological units at the boundaries, we used for the geological map a total amount of 12 tiles (Figure 1).

In addition to the BDRs, we used HIW and HIE basemaps, which include images with high-incidence angles illuminated from the west and east, respectively. These helped us to discern low-relief topography

CONTACT L. Giacomini lorenza.giacomini@inaf.it INAF, Istituto di Astrofisica e Planetologia Spaziali, via Fosso del Cavaliere 100, 00133 Roma, Italy
Supplemental data for this article can be accessed online at https://doi.org/10.1080/17445647.2024.2421600.

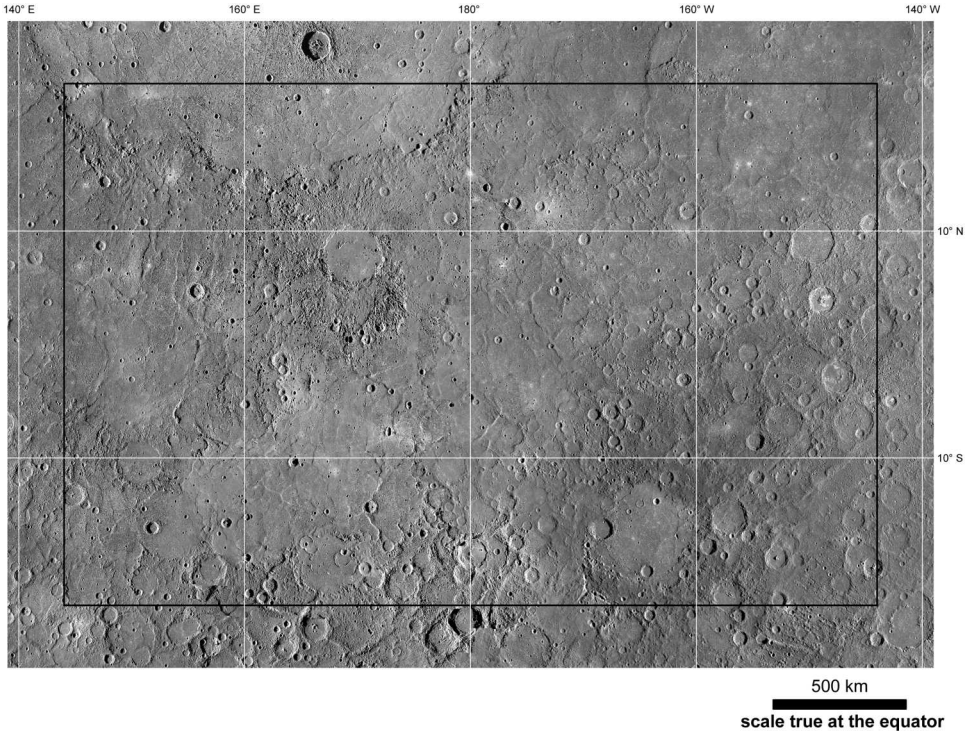

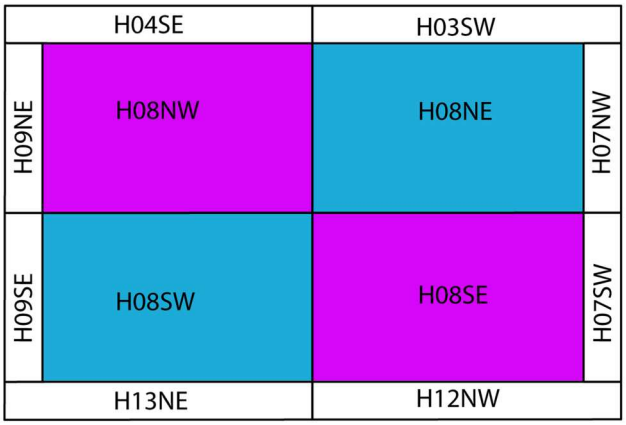

Figure 1. BDR mosaics of Tolstoj quadrangle (H08) used as the main basemap in Mercator projection. Black square indicates the boundary of H08. The basemap has 5° of overlap with the neighbor quadrangles. A total amount of 12 tiles have been used.

(Figure 2a and b). Coupled with the monochrome images, we used the MDIS WAC global color mosaic, both with three and eight colors (Figure 2c and d). Although their spatial resolution (332 m/pixel for the 3 color-mosaic and 665 m/pixel for the 8 color mosaic) did not allow a detailed mapping, the MDIS WAC images were useful mainly to distinguish bright and dark deposits. Also, the Enhanced color mosaic (665 m/pixel) (Figure 2e), which highlights the different color units, was used to identify and map the volcanic deposits and to detect hollow fields.

Finally, the topography of the quadrangle was obtained by the global USGS DTM (Digital Terrain Model) (Figure 2f). It is derived by MDIS WAC and NAC and has a spatial resolution of 665 m/pixel (Becker et al., 2016). The DTM was useful to distinguish the boundaries between smooth and intercrater plains as well as to discern old craters eroded and/or partially buried by subsequent smooth plains.

3. Methods

3.1. Projection and scale

Since the Tolstoj quadrangle is located in the equatorial region, we used the Mercator projection. The reference datum for the projection was the Mercury 2015 (sphere's radius = 2439.4 km). To build the quadrangle mosaic, we projected individual tiles, and then, we mosaicked them using the ISIS (Integrated Software for Imagers and Spectrometers) software. The projected basemaps were imported into the ArcGIS environment, and then, the geological features were

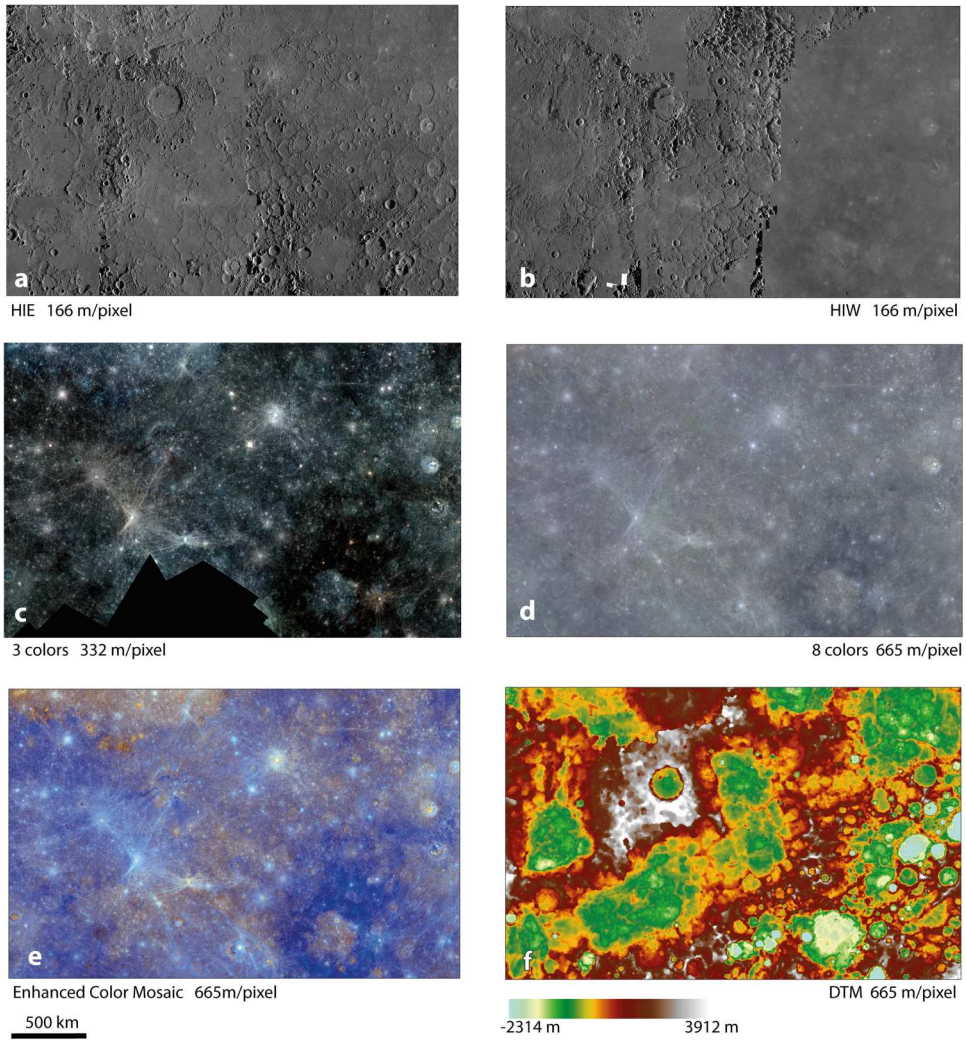

Figure 2. Ancillary basemaps of Tolstoj quadrangle: (a) 166 m/pixel HIE BDR MDIS mosaic; (b) 166 m/pixel HIW BDR MDIS mosaic; (c) 332 m/pixel 3 color MDIS mosaic: R: 1000, G: 750, B: 430 nm; (d) 665 m/pixel 8 color MDIS mosaic: R: 1000, G: 750, B: 430 nm; (e) 665 m/pixel enhanced color mosaic (Denevi et al., 2016); and (f) 665 m/pixel USGS DTM mosaic.

digitalized as vector layers. The map was performed using the standards indicated in the USGS planetary mapping protocol (Skinner et al., 2022). To achieve a final map scale at 1:3.000.000, mapping was performed at a scale of 1:300.000–1:600.000, following Galluzzi et al. (2016).

3.2. Mapping method

To perform the geological map, we consider three feature classes: (i) geological contacts, (ii) lineaments, and (iii) surface features. Geological contacts enclose surfaces with the same characteristics, such as albedo/color, texture and stratigraphic position, defining a geological unit. In the map, we distinguish between 'contact, certain', when the boundary between geological units is neat and clear, and 'contact, approximate', when the boundary is more irregular and blurred. Lineaments include: tectonic structures, crater and pit rims.

Tectonic structures are subdivided into (i) wrinkle ridges, which are low-relief arches with a narrow superposed ridge. They are interpreted to be formed by a combination of folding and thrust faulting (Watters et al., 2009), and they are localized in smooth plains; (ii) thrusts, including lobate scarps and high relief ridges. The former are linear or arcuate in plan view and asymmetric in cross section, characterized by a steep frontal scarp and a gently dipping back slope, whereas the latter are more symmetrical with greater relief than the wrinkle ridges (Watters & Nimmo, 2010); and (iii) graben, which are the surface expression of normal faults with opposing polarity (Watters et al., 2009).

Crater rims define the crest of craters subdivided into two groups based on their diameters: for ≥20 km-diameter craters, the crest has been traced with a continuous line bearing ornamental ticks on the inward sides. Further, these craters are mapped with geological contacts that define their floor and crater material, such as crater wall and central peak or peak ring. For diameters between 20 and 5 km, the crest of craters is traced only with a continuous line, and no geological contacts have been drawn to limit

their floor. Crests of buried and very degraded craters are traced with a dashed line.

Pit rims delineate the edge of irregular depressions interpreted to be volcanic vents.

Finally, surface features include crater chains or clusters, faculae, hollows, bright and dark material. They have been mapped with polygons superposed on the geological units. Only features greater than 10 km were considered. Crater chains or clusters are secondary craters arranged in a raw or in groups. Faculae are diffuse bright red areas (Pegg et al., 2021; Wright et al., 2019) that have been interpreted as explosive volcanic deposits (Gillis-Davis et al., 2009; Goudge et al., 2014; Head et al., 2009; Jozwiak et al., 2018; Kerber et al., 2009, 2011; Murchie et al., 2008; Rothery et al., 2014; Thomas et al., 2014). Hollows are pitted terrain areas likely formed for loss of volatiles, which can occur as a single depression or a group of small pits (Blewett et al., 2011, 2013). Bright materials are high albedo deposits representing the freshest and rayed ejecta, whereas dark materials are interpreted to be low reflectance terrain excavated from depth by impacts (Klima et al., 2018).

3.3. Crater classification

To map craters, two different schemes were used by previous mappers of Mercury's quadrangles: a five-class and a three-class scheme. In the five-class scheme, craters are distinguished based on their morphologies, assigning to each class a stratigraphic position (McCauley et al., 1981, recently reviewed by Kinczyk et al., 2020). However, with this morphological classification, older craters could overlie younger craters. To avoid any conflict between relative ages implied by the degree of crater degradation and their relative stratigraphic ages, in this map, we used a three-class scheme (Figure 3), from c1 to c3. c1 includes the oldest, very degraded, craters, whereas c3 consists of the youngest and freshest craters. c2 includes the craters with intermediate morphologies between the two end-members.

4. Geological map description

4.1. Crater material

c3: craters with sharp morphology. Rims, as well as their central peaks or peak rings, are intact. Crater walls are terraced. Ejecta are extensive; they can reach over 1 diameter of distance from the crater rim and preserve their hummocky textures. They can appear rayed and bright. The boundary between ejecta and the surrounding terrain is clearly visible.

c2: craters with intermediate characteristics between c3 and c1. Rims, central peaks or peak rings are intact but not sharp. Terraces, if present, are not fresh. Ejecta are extended but their boundaries with the surrounding terrain are not clearly detectable.

c1: very eroded craters. Rims are discontinuous, peaks or central peaks are heavily or totally eroded. Ejecta are absent or barely visible in the proximity of the rim.

cfs: crater floor, smooth. The floor is very flat and poorly cratered. On c1 smooth crater floor, it is likely volcanic flows, whereas on c2 and c3, it is probably due to impact melt or lava flows.

cfh: crater floor, hummocky. The floor shows a rough texture, moderately cratered. On c3 and c2, the hummocky floor is likely due to mass wasting deposits, whereas on c1, it is due to degradation, caused by subsequent impacts.

4.2. Caloris basin material

CMF: Caloris Montes Formation. In some areas, it appears as continuous outcrops of rocky terrains; in other regions, it is more discontinuous and has a more knobby appearance. It represents the crater rim of the Caloris basin (Fassett et al., 2009 and McCauley et al., 1981) (Figure 4).

NF: Nervo Formation. It appears as smooth patches bounded by rough or knobby massifs of the Caloris Montes Formation. It was interpreted as impact melt or ejecta blanket (Fassett et al., 2009 and McCauley et al., 1981) (Figure 4).

OF: Odin Formation. It is located radially outside the Caloris rim and includes terrain with knobs of limited dimensions. It is interpreted as ejecta blocks of Caloris, although its origin is still uncertain (e.g. Spudis, 1993) (Figure 4).

VEF: Van Eyck Formation. It is characterized by lineations, represented by a series of ridges and troughs (Fassett et al., 2009) with an orientation subradial from the Caloris rim. In the quadrangle, it extends up to 1000 km southward from the Caloris Montes Formation. It was interpreted as ejecta from Caloris secondaries (Buczkowski et al., 2017) (Figure 4).

4.3. Plains

icp: intercrater plains. Heavily cratered terrain with a rough and hummocky surface texture (Figure 5). No distinctive color is observed for this unit since it shows a shade from yellow to blue. It represents the oldest surface of the quadrangle, dated Tolstojan to pre-Tolstojan in age (> 3.9 Ga; Whitten et al., 2014). The origin of these plains is still debated: they are likely the result of effusive volcanism, although an impact crater origin cannot be excluded (Denevi et al., 2013; Whitten et al., 2014). In H08, the intercrater plains are mapped mainly in the southeastern

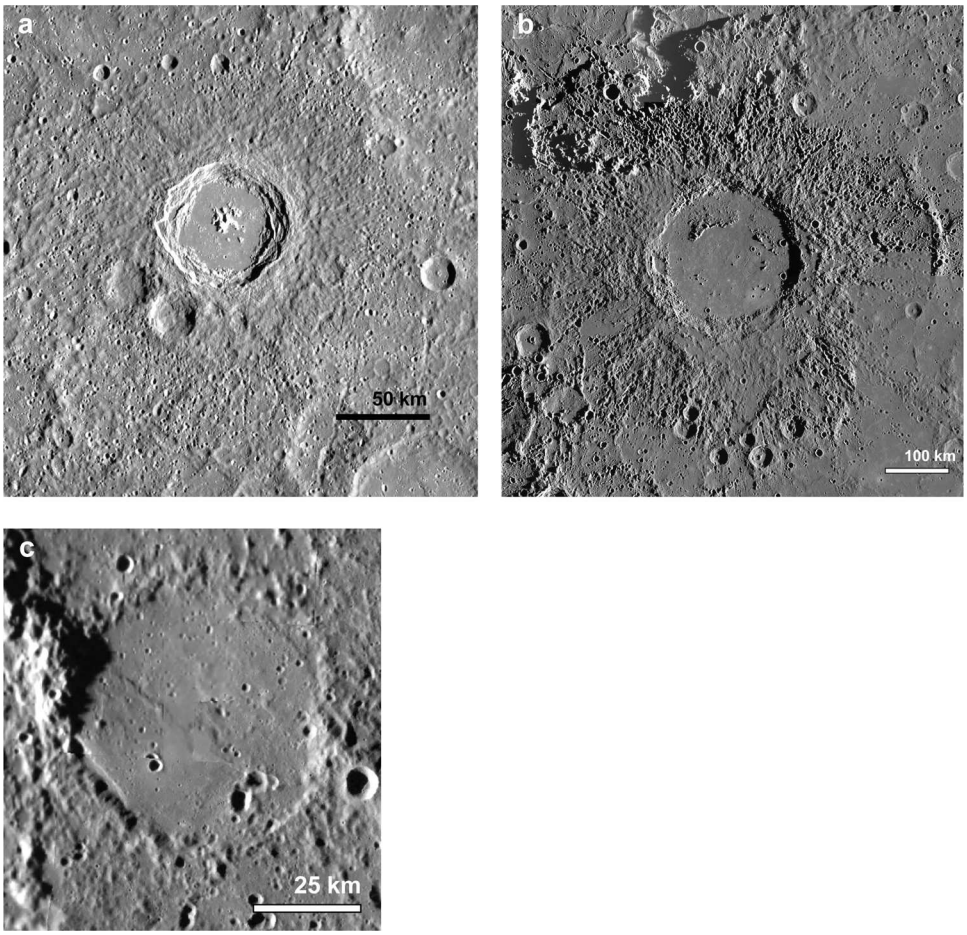

Figure 3. Tolstoj quadrangle 3 crater classes: (a) Balzac crater as an example of c3 crater class; (b) Mozart crater as an example of c2 crater class; and (c) unnamed crater, centered at 154,8°E and 6,9°S, as an example of c1 crater class (see text for more details about the crater classification criteria).

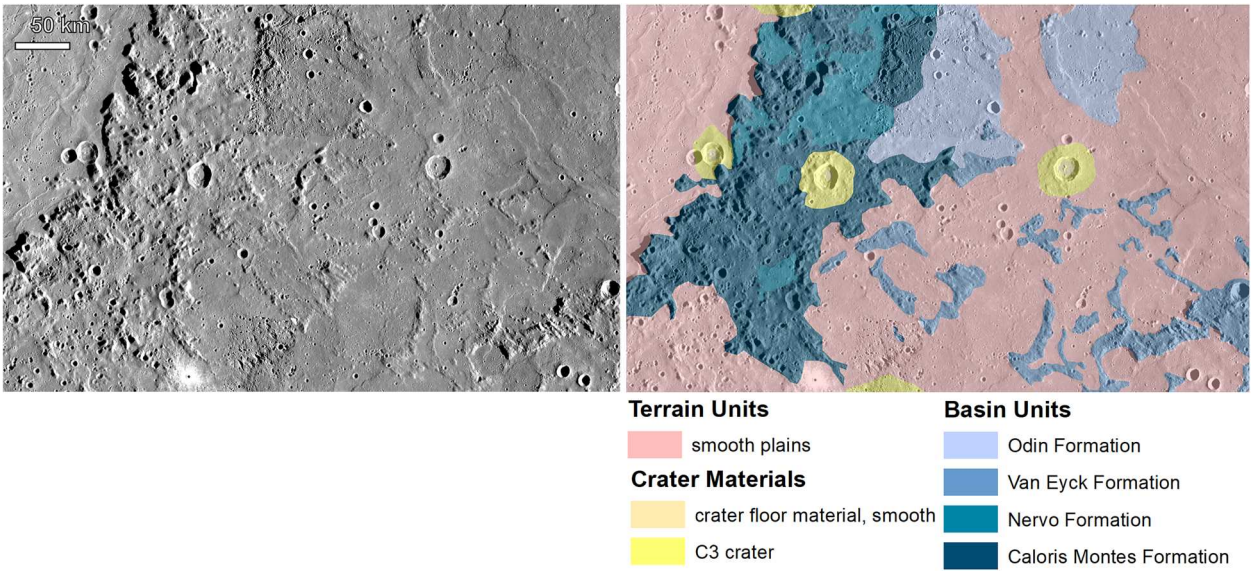

Figure 4. Caloris basin material. On the right panel, Caloris Montes Formation (CMF; knobby surface), Nervo Formation (NF, smooth surface between massifs), Odin Formation (OF; rough surface with sporadic knobs), and Van Eyck Formation (VEF; lineated surface) are shown. See text for more details.

corner of the quadrangle. It is superposed by craters belonging from c1 to c3 class.

imp: intermediate plains. Terrain with intermediate characteristics between intercrater and smooth plains. Indeed, it is less cratered and with a smoother surface texture than intercrater plains but more cratered and with a rougher texture than smooth plains (Figure 6). The boundaries of intermediate plains are frequently

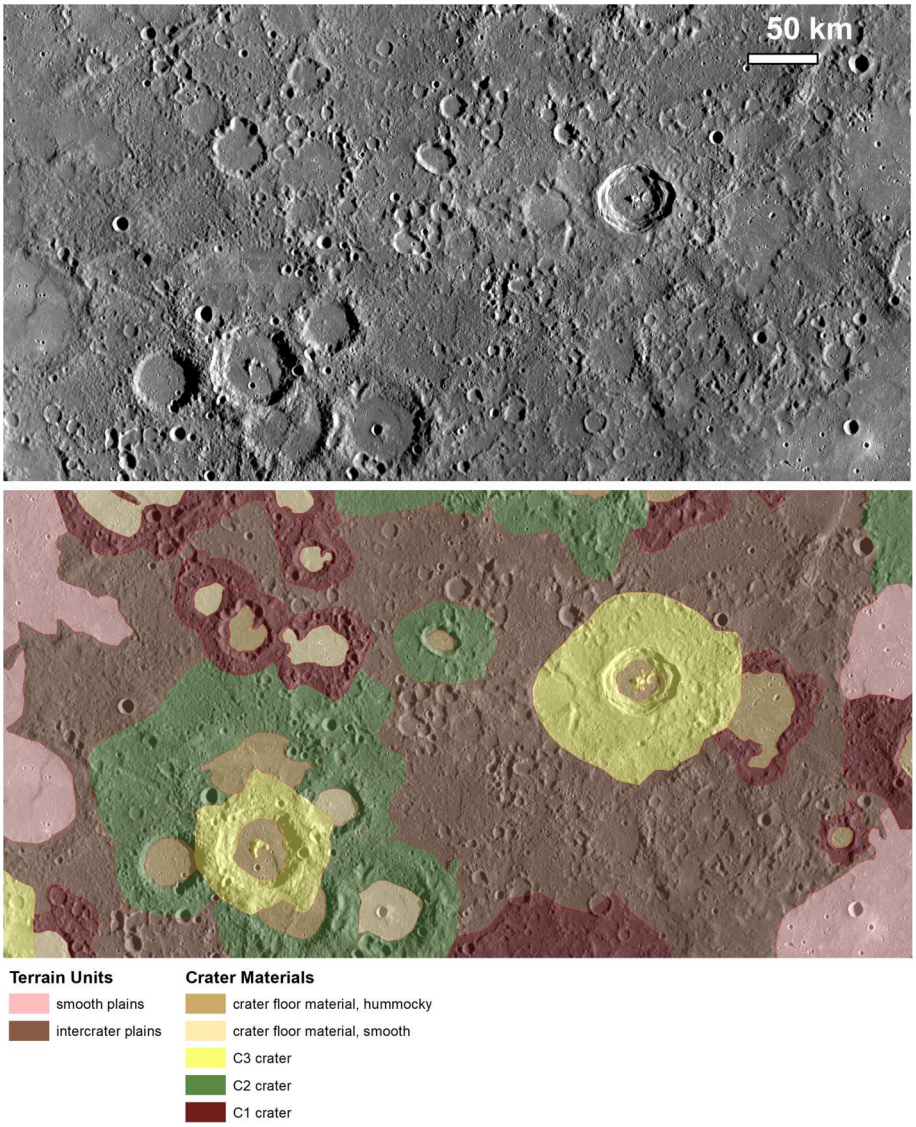

Figure 5. Example of intercrater plains mapped in H08. They are characterized by a rough texture and a very cratered surface.

indistinct. Indeed, a progressive transition with intercrater plains is observed, where smooth deposits cover the underlying intercrater plains progressively filling the terrain depressions and embaying crater rims. Color maps do not help in distinguishing intermediate plains since they do not show a distinctive color with respect to the surroundings. In other quadrangles, the presence of wrinkle ridges helps in distinguishing the intermediate from intercrater plains, since this latter unit lacks such structures (Giacomini et al., 2022). However, wrinkle ridges were not observed in the H08's intermediate plains, likely due to the limited extension of these plains in the quadrangle. Indeed, the existence of intermediate plains as a proper geological unit is still debated. It was introduced during the mapping with Mariner10 images, according to their morphological characteristics (e.g. Grolier & Boyce, 1984; Spudis & Prosser, 1984), whereas Denevi et al. (2009) mentioned an 'intermediate plains' unit distinguished based on its spectral characteristics, which are different from smooth plains and low reflectance material. However, recently, Whitten et al. (2014) argue that intermediate plains are composed both by intercrater and by smooth plains, and therefore, they would be included in the latter group. In this work, in accordance with the previous mappers (Galluzzi et al., 2016; Giacomini et al., 2022; Guzzetta et al., 2017; Malliband et al., 2023; Man et al., 2023; Mancinelli et al., 2016; Pegg et al., 2021; Wright et al., 2019), we kept intermediate plains as a distinct unit, referring mainly to their morphological characteristics. The terrain is superposed by c2 and c3 craters.

sp: smooth plains. Poorly cratered terrain with a smooth texture (Figure 7). Smooth plains represent the most extended units of H08. They are emplaced both inside and outside the Caloris basin. Smooth plains are affected by wrinkle ridges. On the smooth plains emplaced within the Caloris floor, wrinkle ridges appear to have both a concentric and radial orientation with respect to the basin center. In the smooth plains outside the Caloris' rim wrinkle ridges preserve a preferential concentric and radial orientation, although

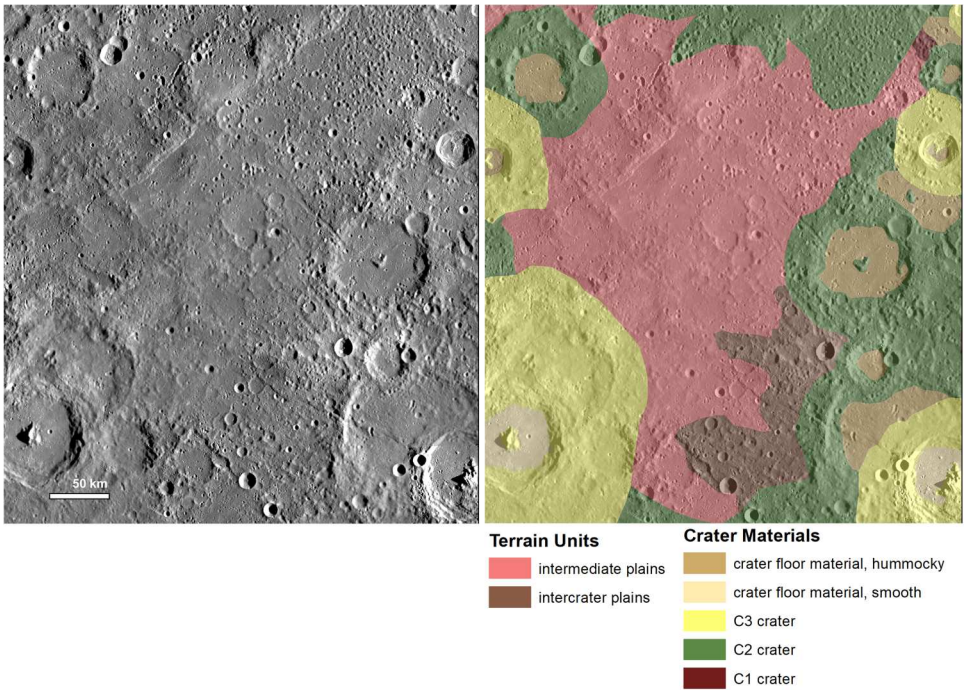

Figure 6. Example of intermediate plains mapped in H08. These plains show intermediate characteristics between intercrater and smooth plains: they are characterized by a rough surface but less rough than the intercrater ones. They are also cratered but less than intercrater plains and more than smooth ones.

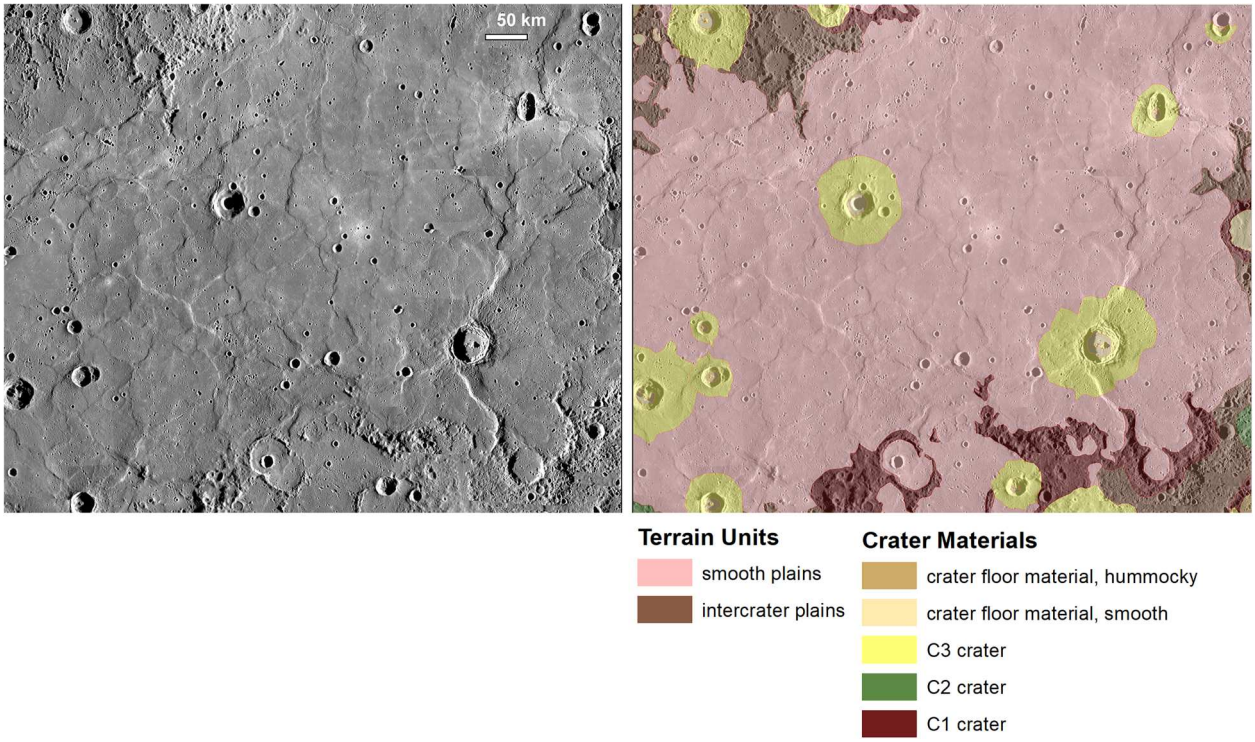

Figure 7. Example of smooth plains mapped in H08. They are poorly cratered and show a smooth surface texture.

several more randomly oriented wrinkle ridges were also observed. Moreover, in the smooth plains inside Caloris, several grabens were mapped. They show both radial and concentric orientation with respect to the Apollodorus crater, located in the proximity of the Caloris' basin center (in the H04 quadrangle). The relationship between grabens and wrinkle ridges is still uncertain. Grabens seem to crosscut, and post-date, wrinkle ridges (Watters et al., 2009). This would imply that the compressional deformation occurring in the smooth plains inside the basin predates the extensions that formed the grabens (Watters et al., 2009). However, for other authors (Basilevsky et al., 2011), this is true only for concentric grabens, while

radial grabens seem to predate the wrinkle ridges, suggesting a more complex deformational history.

Smooth plains are not limited to the Caloris basin areas. Indeed, they fill also the major crater floors (e.g. Tolstoj crater) of the quadrangle. The origin of smooth plains is attributed to recent effusive volcanism, Calorian in age (3.7–3.9 Ga) (Denevi et al., 2013; Fassett et al., 2009; Head et al., 2011; Strom et al., 2008, 2011). This terrain is superposed by c2 and c3 craters.

Small patches of smooth plains have been mapped around some of the larger craters (i.e. Mozart, Tyagaraja, and Zeami craters) and they have been interpreted to be ponds of impact melt (Wright et al., 2019).

4.4. Units' age

To establish the stratigraphic relationship between the different geological units, we dated them through the crater counting method, as described by the Crater Analysis Techniques Working Group (1979). We chose six sample regions: one for intercrater plains, two intermediate plains and three samples for smooth plains (Figure 8a).

The obtained counts were arranged in a cumulative size frequency distribution (CSFD). The different CSFDs were compared to each other to establish their relative ages (Figure 8b). Subsequently, they were related with the Le Feuvre and Wiekzoreck Production Function (LWPF) (2011) to estimate their absolute model age (Figure 8c–h)

For the intercrater plains, we obtained an age of 3.8 (+0.01–0.02) Ga (Figure 8h), confirming that it is the oldest unit in the quadrangle. To date this surface, we used the non-porous scaling law, since the craters considered for the best fit with LWPF have a large diameter. Therefore, hard rock terrain is involved. Smooth plains emplaced within and around the Caloris basin have been dated at about 3.7 Ga (Figure 8c–e), in accordance with previous authors (Denevi et al., 2013; Fassett et al., 2009; Strom et al., 2008). In this case, the porous scaling law was used due to the modest dimension of craters that affected only the upper surface, which is likely fractured both by subsequent impacts and by lava flows cooling (Giacomini et al., 2020; Schultz, 1993). The age-consistency among the three smooth plains sample areas, taken both inside and outside the Caloris basin, seems to support the hypothesis of a continuity between the basin's interior and exterior plains (Rothery et al., 2017), as further confirmed by our map showing no boundaries between the two plains in correspondence of the gaps of Caloris basin's rim.

The stratigraphic position of the intermediate plains is instead less clear. Indeed, one sample region (Intermediate 1) was dated at 3.8 (+0.07–0.02) Ga (Figure 8g), whereas the other sample area (intermediate 2) was dated at about 3.7 (+0.02–0.04) Ga (Figure 8f). For both areas, a porous scaling law was used for the same reasons described for the smooth plains. The possible explanation of this variable age is that intermediate plains are intercrater plains progressively flooded by smooth deposits that, however, did not completely bury the underlying terrain. In the case of intermediate 1, smooth deposits are quite thin, and therefore, the crater rims are still visible and were counted in the dating process, returning an age like the intercrater plains. In the case of intermediate 2, the smooth deposits are thick enough to cover a great part of the underlying craters; therefore, its age is more comparable to the smooth plains age.

On the basis of the stratigraphic position observed between the different geologic units and of the absolute age obtained in this work and estimated by previous authors (Byrne et al., 2016; Marchi et al., 2013; Neukum et al., 2001; Ostrach et al., 2015; Whitten et al., 2014), we propose the stratigraphic scheme as shown in Figure 9.

5. Conclusions

We compiled the geological map of the Tolstoj quadrangle (H08) of Mercury at a scale of 1:3M using MESSENGER data. This represents a more detailed and complete map than the previous one performed at a scale of 1:5M with Mariner10 data that covers only the eastern sector of the quadrangle. Indeed, the higher resolution of MESSENGER MDIS data allowed a better definition of the geological units' boundaries. This is particularly evident for the units related to Caloris basin (i.e. Caloris Montes, Nervo, Van Eyck, Odin Formation), whose extension were better established since high spatial resolution permits to distinguish their surface textures more accurately. The method used for the mapping follows the one defined by the quadrangle geological maps already published at the same scale (Galluzzi et al., 2016; Giacomini et al., 2022; Guzzetta et al., 2017; Malliband et al., 2023; Man et al., 2023; Mancinelli et al., 2016; Pegg et al., 2021; Wright et al., 2019). The map highlights as Caloris basin and its related features dominate the quadrangle. Indeed, the southern part of the basin rim is located in the northwestern area of H08 and the smooth plains emplaced within and all around the basin rim cover a great part of the quadrangle. On the contrary, intercrater plains are confined in the southeastern sector of H08 and are less extended. This map is part of a wider project devoted to the global mapping of Mercury's surface (Galluzzi et al., 2024).

Software

To produce our map, we used Esri ArcGIS Desktop 10.8.2 software. Some images have been processed

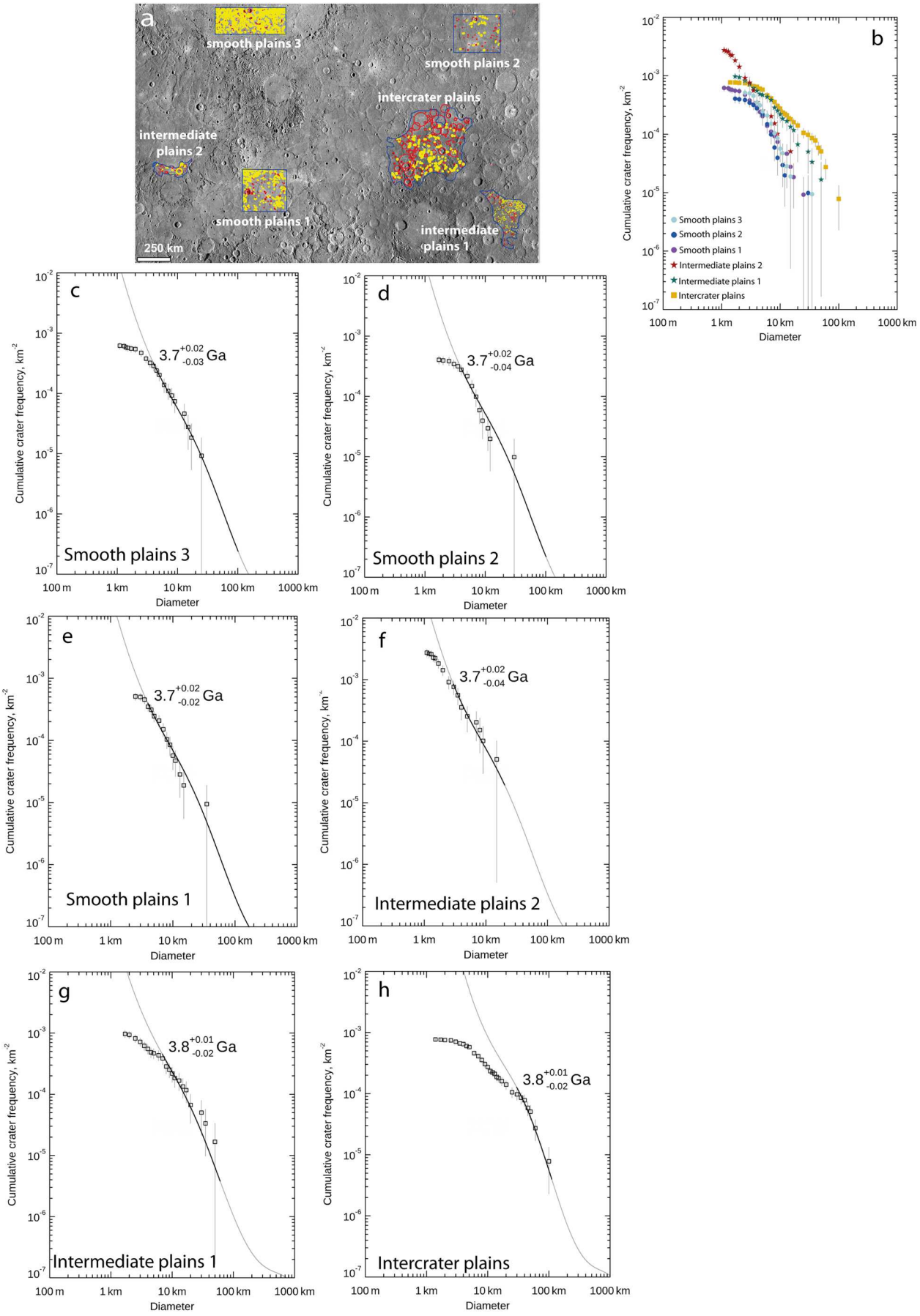

Figure 8. Results of crater counting performed on H08. We considered three smooth plains, two intermediate plains and one intercrater plains (a). Plot of the obtained crater-size frequency distributions (CFSDs) to estimate their relative age (b). Absolute model age for the surface, derived from the comparison with Le Feuvre and Wiekzoreck Production Function (c–h).

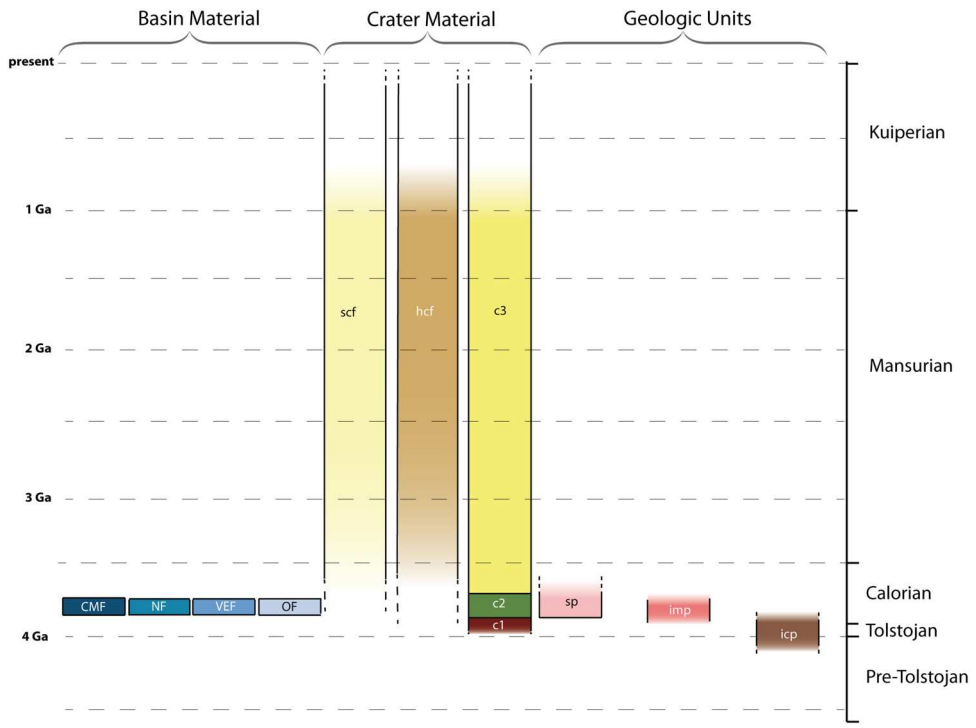

Figure 9. Stratigraphic scheme of H08 map units based on superposition relations and the estimated ages of sp, imp and icp from the literature (Byrne et al., 2016; Marchi et al., 2013; Neukum et al., 2001; Ostrach et al., 2015; Whitten et al., 2014). Basal ages for the chrono-stratigraphic systems are from Spudis and Guest (1988).

using ISIS3 (Integrated Software for Imagers and Spectrometers v3) software (Eliason, 1997; Gaddis et al., 1997; Torson & Becker, 1997), developed by the USGS (United States Geological Survey). To perform the crater counting, we used Crater Tools (Kneissl, Van Gasselt, & Neukum, 2011), whereas to plot the results of the counts, we used the Craterstats2 (e.g. see Michael & Neukum, 2010).

Acknowledgments

The authors thank D.A. Rothery, G. Tognon and M. Murad-al-shaikh who provided detailed and helpful suggestions that improved the quality of the manuscript and map. The authors acknowledge the use of MESSENGER data processed by NASA/Johns Hopkins University Applied Physics Laboratory/Carnegie Institution of Washington.

Disclosure statement

No potential conflict of interest was reported by the author(s).

Funding

Part of this work was funding from the Agenzia Spaziale Italiana under ASI-INAF agreement 2017-47-H.0.

Data availability statement

The data and materials that support the results of this work are freely available upon reasonable request.

ORCID

L. Guzzetta http://orcid.org/0000-0003-3619-1032

References

Basilevsky, A. T., Head, J. W., Fassett, C. I., & Michael, G. (2011). History of tectonic deformation in the interior plains of the Caloris basin, Mercury. *Solar System Research*, *45*(6), 471–497. https://doi.org/10.1134/S0038094611060025

Becker, K., Robinson, M., Becker, T., Weller, L., Edmundson, K., Neumann, G., Perry, M., & Solomon, S. (2016). First global digital elevation model of Mercury. *Lunar and Planetary Science Conference, 2959*, Abstract No. 1903.

Blewett, D. T., Chabot, N. L., Denevi, B. W., Ernst, C. M., Head, J. W., Izenberg, N. R., Murchie, S. L., Solomon, S. C., Nittler, L. R., McCoy, T. J., Xiao, Z., Baker, D. M. H., Fassett, C. I., Braden, S. E., Oberst, J., Scholten, F., Preusker, F., & Hurwitz, D. M. (2011). Hollows on Mercury: MESSENGER evidence for geologically recent volatile-related activity. *Science*, *333*(6051), 1856–1859. https://doi.org/10.1126/science.1211681

Blewett, D. T., Vaughan, W. M., Xiao, Z., Chabot, N. L., Denevi, B. W., Ernst, C. M., Helbert, J., D'Amore, M., Maturilli, A., Head, J. W., & Solomon, S. C. (2013). Mercury's hollows: Constraints on formation and composition from analysis of geological setting and spectral reflectance. *Journal of Geophysical Research: Planets*, *118*(5), 1013–1032. https://doi.org/10.1029/2012JE004174

Buczkowski, D. L., Goosmann, E., Denevi, B. W., Ernst, C. M., Fassett, C. I., & Byrne, P. K. (2017). *A Geologic Map of the Caloris Basin, Mercury*. Third Planetary Data Workshop and The Planetary Geologic Mappers Annual Meeting, Arizona, No. 1986, id.7109.

Byrne, P. K., Ostrach, L. R., Fassett, C. I., Chapman, C. R., Denevi, B. W., Evans, A. J., Klimczak, C., Banks, M. E., Head, J. W., & Solomon, S. C. (2016). Widespread effusive volcanism on Mercury likely ended by about

3.5Ga. *Geophysical Research Letters*, *43*(14), 7408–7416. https://doi.org/10.1002/2016GL069412

Crater Analysis Techniques Working Group. (1979). Standard techniques for presentation and analysis of crater size-frequency data. *Icarus*, *37*(2), 467–474. https://doi.org/10.1016/0019-1035(79)90009-5.

De Hon, R. A., Scott, D. H., & Underwood, J. R. J. (1981). *Geologic map of the Kuiper (h-6) quadrangle of Mercury*. USGS Miscellaneous Investigations Series Map I-1233.

Denevi, B. W., Ernst, C. M., Meyer, H. M., Robinson, M. S., Murchie, S. L., Whitten, J. L., Head, J. W., Watters, T. R., Solomon, S. C., Ostrach, L. R., Chapman, C. R., Byrne, P. K., Klimczak, C., & Peplowski, P. N. (2013). The distribution and origin of smooth plains on Mercury. *Journal of Geophysical Research: Planets*, *118*(5), 891–907. https://doi.org/10.1002/jgre.20075

Denevi, B. W., Ernst, C. M., Prockter, L. M., Robinson, M. S., Spudis, P. D., Klima, R. L., & Kinczyk, M. J. (2016). The origin of Mercury's oldest surfaces and the nature of intercrater plains resurfacing. *Lunar and Planetary Science Conference*, 47th, #1624, bibcode: 2016LPI…47.1624D.

Denevi, B. W., Robinson, M. S., Solomon, S. C., Murchie, S. L., Blewett, D. T., Domingue, D. L., McCoy, T. J., Ernst, C. M., Head, J. W., Watters, T. R., & Chabot, N. L. (2009). The evolution of Mercury's crust: A global perspective from MESSENGER. *Science*, *324*(*5927*), 613–618. http://doi.org/10.1126/science.1172226

Eliason, E. M. (1997). Production of digital image models using the ISIS system. *Lunar and Planetary Science Conference*, p. 331, 1997LPI....28..331E.

Fassett, C. I., Head, J. W., Blewett, D. T., Chapman, C. R., Dickson, J. L., Murchie, S. L., Solomon, S. C., & Watters, T. R. (2009). Caloris impact basin: Exterior geomorphology, stratigraphy, morphometry, radial sculpture, and smooth plains deposits. *Earth and Planetary Science Letters*, *285*(3), 297–308. https://doi.org/10.1016/j.epsl.2009.05.022

Gaddis, L., Anderson, J., Becker, K., Becker, T., Cook, D., Edwards, K., Eliason, E., Hare, T., Kieffer, H., Lee, E. M., Mathews, J., Soderblom, L., Sucharski, T., Torson, J., Mcewen, A. (1997). *An overview of the integrated software for imaging spectrometers (ISIS)*. Lunar and Planetary Science Conference, p. 387, 1997LPI....28..387G.

Galluzzi, V., Guzzetta, L., Ferranti, F., Di Achille, G., Rothery, D. A., & Palumbo, P. (2016). Geology of the Victoria quadrangle (H02), Mercury. *Journal of Maps*, *12*(sup1), 227–238. https://doi.org/10.1080/17445647.2016.1193777

Galluzzi, V., Rothery, D. A., Blance, A., Giacomini, L., Guzzetta, L., Lennox, A. R., Man, B., Sepe, A., Tognon, G., Wright, J., Massironi, M., & Ferranti, L. (2024). Update on the Quadrangle Geological Map Series of Mercury. *Mercury 2024*, abstract, 2024.

Giacomini, L., Galluzzi, V., Massironi, M., Ferranti, L., & Palumbo, P. (2022). Geology of the Kuiper quadrangle (H06), Mercury. *Journal of Maps*, *18*(2), 246–257. https://doi.org/10.1080/17445647.2022.2035268

Giacomini, L., Massironi, M., Galluzzi, V., Ferrari, S., & Palumbo, P. (2020). How old are the Mercury's thrust systems? *New clues on the thermal evolution of the planet. Geoscience Frontiers*, *11*(3), 855–870.

Gillis-Davis, J. J., Blewett, D. T., Gaskell, R. W., Denevi, B. W., Robinson, M. S., Strom, R. G., Solomon, S. C., & Sprague, A. L. (2009). Pit-floor craters on Mercury: Evidence of near-surface igneous activity. *Earth and Planetary Science Letters*, *285*(3-4), 243–250. https://doi.org/10.1016/j.epsl.2009.05.023

Goudge, T. A., Head, J. W., Kerber, L., Blewett, D. T., Denevi, B. W., Domingue, D. L., Gillis-Davis, J. J., Gwinner, K., Helbert, J., Holsclaw, G. M., Izenberg, N. R., Klima, R. L., McClintock, W. E., Murchie, S. L., Neumann, G. A., Smith, D. E., Strom, R. G., Xiao, Z., Zuber, M. T., … Solomon, S. C. (2014). Global inventory and characterization of pyroclastic deposits on Mercury: New insights into pyroclastic activity from MESSENGER orbital data. *Journal of Geophysical Research: Planets*, *119*(*3*), 635–658. http://doi.org/10.1002/jgre.v119.3

Grolier, M. J., & Boyce, J. M. (1984). *Geologic map of the Borealis region (H-1) of Mercury*. USGS Miscellaneous Investigations Series Map I–1660 1–1.

Guest, J. E., & Greeley, R. (1983). *Geologic map of the Shakespeare quadrangle of Mercury*. USGS Miscellaneous Investigations Series Map I-1408.

Guzzetta, L., Galluzzi, V., Ferranti, L., & Palumbo, P. (2017). Geology of the Shakespeare quadrangle (H03), Mercury. *Journal of Maps*, *13*(2), 227–238. https://doi.org/10.1080/17445647.2017.1290556

Head, J. W., Chapman, C. R., Strom, R. G., Fassett, C. I., Denevi, B. W., Blewett, D. T., Ernst, C. M., Watters, T. R., Solomon, S. C., Murchie, S. L., Prockter, L. M., Chabot, N. L., Gillis-Davis, J. J., Whitten, J. L., Goudge, T. A., Baker, D. M. H., Hurwitz, D. M., Ostrach, L. R., Xiao, Z., … Nittler, L. R. (2011). Flood volcanism in the northern high latitudes of Mercury revealed by MESSENGER. *Science*, *333*(6051), 1853–1856. https://doi.org/10.1126/science.1211997

Head, J. W., Murchie, S. L., Prockter, L. M., Solomon, S. C., Chapman, C. R., Strom, R. G., Watters Thomas R., Blewett David T., Gillis-Davis Jeffrey J., Fassett Caleb I., Dickson James L., Morgan Gareth A., & Kerber, L. (2009). Volcanism on Mercury: Evidence from the first MESSENGER flyby for extrusive and explosive activity and the volcanic origin of plains. *Earth and Planetary Science Letters*, *285*(3-4), 227–242. https://doi.org/10.1016/j.epsl.2009.03.007

Jozwiak, L. M., Head, J. W., & Wilson, L. (2018). Explosive volcanism on Mercury: Analysis of vent and deposit morphology and modes of eruption. *Icarus*, *302*, 191–212. https://doi.org/10.1016/j.icarus.2017.11.011

Kerber, L., Head, J. W., Blewett, D. T., Solomon, S. C., Wilson, L., Murchie, S. L., Robinson, M. S., Denevi, B. W., & Domingue, D. L. (2011). The global distribution of pyroclastic deposits on Mercury: The view from MESSENGER flybys 1-3. *Planetary and Space Science*, *59*(15), 1895–1909. https://doi.org/10.1016/j.pss.2011.03.020

Kerber, L., Head, J. W., Solomon, S. C., Murchie, S. L., Blewett, D. T., & Wilson, L. (2009). Explosive volcanic eruptions on Mercury: Eruption conditions, magma volatile content, and implications for interior volatile abundances. *Earth and Planetary Science Letters*, *285*(3-4), 263–271. https://doi.org/10.1016/j.epsl.2009.04.037

Kinczyk, M. J., Prockter, L. M., Byrne, P. K., Denevi, B. W., Buczkowski, D. L., Ostrach, L. R., & Miller, E. B. (2019). The first global geological map of Mercury. *EPSC-DPS Joint Meeting*, *13*, 1045.

Kinczyk, M. J., Prockter, L. M., Byrne, P. K., Susorney, H. C. M., & Chapman, C. R. (2020). A morphological evaluation of crater degradation on Mercury: Revisiting crater classification with MESSENGER data. *Icarus, 341*, 113637. https://doi.org/10.1016/j.icarus.2020.113637.

King, J. S., & Scott, D. H. (1990). *Geologic map of the Beethoven quadrangle of Mercury*. USGS Miscellaneous Investigations Series Map I-2048.

Klima, R. L., Denevi, B. W., Ernst, C. M., Murchie, S. L., & Peplowski, P. N. (2018). Global Distribution and Spectral Properties of Low-Reflectance Material on Mercury. *Geophysical Research Letters*, *45*(7), 2945–2953. https://doi.org/10.1002/2018GL077544

Kneissl, T, van Gasselt, S., & Neukum, G. (2011). Map-projection-independent crater size-frequency determination in GIS environments—New software tool for ArcGIS. *Planetary and Space Science*, *59*(*11-12*), 1243–1254. http://doi.org/10.1016/j.pss.2010.03.015

Le Feuvre, M., & Wieczorek, M. A. (2011). Nonuniform cratering of the Moon and a revised crater chronology of the inner Solar System. *Icarus*, *214*(1), 1–20. https://doi.org/10.1016/j.icarus.2011.03.010

Malliband, C. C., Rothery, D. A., Balme, M. R., Conway, S. J., Pegg, D. L., & Wright, J. (2023). Geology of the Derain quadrangle (H10), Mercury. *Journal of Maps*, *19*(1), 1–10. https://doi.org/10.1080/17445647.2022.2112774

Man, B., Rothery, D. A., Balme, M. R., Conway, S. J., Wright, J., Pegg, D. L., Lennox, A. R., & Buoninfante, S. (2023). Geology of the Neruda quadrangle (H13), Mercury. *Journal of Maps*, *19*(1), 2023. https://doi.org/10.1080/17445647.2023.2256353

Mancinelli, P., Minelli, F., Pauselli, C., & Federico, C. (2016). Geology of the raditladi quadrangle, Mercury (H04). *Journal of Maps*, *5647*, 1–13.

Marchi, S., Chapman, C. R., Fassett, C. I., Head, J. W., Bottke, W. F., & Strom, R. G. (2013). Global resurfacing of Mercury 4.0–4.1 billion years ago by heavy bombardment and volcanism. *Nature*, *499*(7456), 59–61. https://doi.org/10.1038/nature12280

McCauley, J. F., Guest, J. E., Schaber, G. G., Trask, N. J., & Greeley, R. (1981). Stratigraphy of the Caloris basin, Mercury. *Icarus*, *47*(2), 184–202. https://doi.org/10.1016/0019-1035(81)90166-4

McGill, G. E., & King, E. A. (1983). USGS Misc. Investig. Ser., Map I-1409.

Michael, G. G., & Neukum, G. (2010). Planetary surface dating from crater size–frequency distribution measurements: Partial resurfacing events and statistical age uncertainty. *Earth and Planetary Science Letters*, *294*(*3-4*), 223–229. http://doi.org/10.1016/j.epsl.2009.12.041

Murchie, S. L., Watters, T. R., Robinson, M. S., Head, J. W., Strom, R. G., Chapman, C. R., Solomon, S. C., McClintock, W. E., Prockter, L. M., Domingue, D. L., & Blewett, D. T. (2008). Geology of the Caloris basin, Mercury: A view from MESSENGER. *Science*, *321* (5885), 73–76. https://doi.org/10.1126/science.1159261

Neukum, G., Oberst, J., Hoffmann, H., Wagner, R., & Ivanov, B. A. (2001). Geologic evolution and cratering history of Mercury. *Planetary and Space Science*, *49*(14-15), 1507–1521. https://doi.org/10.1016/S0032-0633(01)00089-7

Ostrach, L. R., Robinson, M. S., Whitten, J. L., Fassett, C. I., Strom, R. G., Head, J. W., & Solomon, S. C. (2015). Extent, age, and resurfacing history of the northern smooth plains on Mercury from MESSENGER observations. *Icarus*, *250*, 602–622. https://doi.org/10.1016/j.icarus.2014.11.010

Pegg, D. L., Rothery, D. A., Balme, M. R., Conway, S. J., Malliband, C. C., & Man, B. (2021). Geology of the Debussy quadrangle (H14), Mercury. *Journal of Maps*, *17*(2), 859–870.

Rothery, D. A., Mancinelli, P., Guzzetta, L., & Wright, J. (2017). Mercury's Caloris basin: Continuity between the interior and exterior plains. *Journal of Geophysical Research: Planets*, *122*(3), 560–576. https://doi.org/10.1002/2017JE005282

Rothery, D. A., Thomas, R. J., & Kerber, L. (2014). Prolonged eruptive history of a compound volcano on Mercury: Volcanic and tectonic implications. *Earth and Planetary Science Letters*, *385*, 59–67. https://doi.org/10.1016/j.epsl.2013.10.023

Schaber, G. G., & McCauley, M. (1980). *Geologic map of the Tolstoj Quadrangle of Mercury*. USGS Miscellaneous Investigations Series Map I-1199.

Schultz, R. A. (1993). Brittle Strength of Basaltic Rock Masses with Applications to Venus. *Journal of Geophysical Research: Planets*, *98*(E6), 10883–10895. https://doi.org/10.1029/93JE00691

Skinner, J. A., Huff, A. E., Black, S. R., Buban, H. C., Fortezzo, C. M., Gaither, T. A., Hare, T. M., & Hunter, M. A. (2022). *Planetary geologic mapping protocol — 2022* (Vol. 11-B13).

Spudis, P. D. (1993). *The Geology of Multi-Ring Impact Basins*. Cambridge University Press. 263 pp.

Spudis, P. D., & Guest, J. E. (1988). Stratigraphy and geologic history of Mercury. In F. Vilas, C. R. Chapman, & M. S. Matthews (Eds.), *Mercury* (pp. 118–164). University of Arizona Press. ISBN: 0816510857.

Spudis, P. D., & Prosser, J. G. (1984). *Geologic map of the Michaelangelo (H-12) Quadrangle of Mercury*. USGS Miscellaneous Investigations Series Map I-1659.

Strom, R. G., Banks, M. E., Chapman, C. R., Fassett, C. I., Forde, J. A., Head, I. I. I. J. W., Merline, W. J., Prockter, L. M., & Solomon, S. C. (2011). Mercury crater statistics from MESSENGER flybys: Implications for stratigraphy and resurfacing history. *Planetary and Space Science*, *59* (15), 1960–1967. https://doi.org/10.1016/j.pss.2011.03.018

Strom, R. G., Chapman, C. R., Merline, W. J., Solomon, S. C., & Head, J. W. (2008). Mercury cratering record viewed from MESSENGER's first flyby. *Science*, *321* (5885), 79–81. https://doi.org/10.1126/science.1159317

Strom, R. G., Malin, M. C., & Leake, M. A. (1990). *Geologic map of the Bach (H-15) quadrangle of Mercury*. USGS Miscellaneous Investigations Series Map I-2015.

Thomas, R. J., Rothery, D. A., Conway, S. J., & Anand, M. (2014). Mechanisms of explosive volcanism on Mercury: Implications from its global distribution and morphology. *Journal of Geophysical Research: Planets*, *119*(10), 2239–2254. https://doi.org/10.1002/2014JE004692

Torson, J. M., & Becker, K. J. (1997). *ISIS - a software architecture for processing planetary images*. Lunar and Planetary Science Conference, p. 1443, 1997LPI....28.1443T.

Trask, N. J., & Dzurisin, D. (1984). *Geologic map of the Discovery quadrangle of Mercury*. USGS Miscellaneous Investigations Series Map I-1658.

Watters, T. R., & Nimmo, F. (2010). Tectonism on Mercury. In R. A. Schultz & T. R. Watters (Eds.), *Planetary Tectonics* (pp. 15–80). Cambridge Univ Press.

Watters, T. R., Solomon, S. C., Robinson, M. S., Head, J. W., André, S. L., Hauck IIS. A., & Murchie, S. L. (2009). The tectonics of Mercury: The view after MESSENGER's first flyby. *Earth and Planetary Science Letters*, *285*(3-4), 283–296. https://doi.org/10.1016/j.epsl.2009.01.025

Whitten, J. L., Head, J. W., Denevi, B. W., & Solomon, S. C. (2014). Intercrater plains on Mercury: Insights into unit definition, characterization, and origin from MESSENGER datasets. *Icarus*, *241*, 97–113. https://doi.org/10.1016/j.icarus.2014.06.013

Wright, J., Rothery, D. A., Balme, M. R., & Conway, S. J. (2019). Geology of the Hokusai quadrangle (H05), Mercury. *Journal of Maps*, *15*(2), 509–520. https://doi.org/10.1080/17445647.2019.1625821